20. G. Nolet, S. P. Grand, B. L. N. Kennett, *J. Geophys. Res.* **99**, 23753 (1994).
21. S. M. Rigden, G. D. Gwanmesia, R. C. Liebermann, *Phys. Earth Planet. Inter.* **86**, 35 (1994).
22. L. Flesch, B. Li, R. C. Liebermann, *Am. Mineral.* **83**, 444 (1998).
23. S. M. Rigden, G. D. Gwanmesia, J. D. FitzGerald, I. Jackson, R. C. Liebermann, *Nature* **354**, 143 (1991).
24. The seismic velocity-depth profiles we used for comparison are in the following references. GCA: M. C. Walck, *Geophys. J. R. Astron. Soc.* **76**, 697 (1984); SNA and TNA: S. Grand, and D. Helmberger, *ibid.*, p. 399; and S25: L. V. LeFevre and D. Helmberger, *J. Geophy. Res.* **94**, 17749 (1989).
25. J. Revenaugh and T. H. Jordan, *J. Geophys. Res.* **96**, 19781 (1991).
26. J. B. Gaherty, P. Puster, T. H. Jordan, Y. Wang, D. J. Weidner, *Eos* **78**, F486 (1997).
27. L. Stixrude, *J. Geophy. Res.* **102**, 14835 (1997).
28. D. J. Weidner *et al.*, in (*6*), pp. 13–17.
29. We thank all those who contributed to the implementation of these ultrasonic experiments in SAM 85 on the X17B1 beamline of the NSLS at Brookhaven National Laboratory and J. B. Hastings and D. P. Siddons at the NSLS for their technical support. Support was from the State University of New York at Stony Brook and from the NSF Science and Technology Center for High Pressure Research (grant EAR89-20239 and NSF grants EAR93-04502 and EAR96-14612 to R.C.L.). This is Mineral Physics Institute contribution number 229.

18 March 1998; accepted 1 June 1998

Ultrasonic Shear Wave Velocities of $MgSiO_3$ Perovskite at 8 GPa and 800 K and Lower Mantle Composition

Yegor D. Sinelnikov,* Ganglin Chen, Daniel R. Neuville, Michael T. Vaughan, Robert C. Liebermann

Ultrasonic interferometric measurements of the shear elastic properties of $MgSiO_3$ perovskite were conducted on three polycrystalline specimens at conditions up to pressures of 8 gigapascals and temperatures of 800 kelvin. The acoustic measurements produced the pressure (P) and temperature (T) derivatives of the shear modulus (G), namely $(\partial G/\partial P)_T = 1.8 \pm 0.4$ and $(\partial G/\partial T)_P = -2.9 \pm 0.3 \times 10^{-2}$ gigapascals per kelvin. Combining these derivatives with the derivatives that were measured for the bulk modulus and thermal expansion of $MgSiO_3$ perovskite provided data that suggest lower mantle compositions between pyrolite and C1 carbonaceous chondrite and a lower mantle potential temperature of 1500 ± 200 kelvin.

Experimental and theoretical efforts have focused on determining the elastic behavior of $(Mg,Fe)SiO_3$ perovskite, the most abundant mineral in Earth's lower mantle, because its physical properties constrain the chemical composition and rheology of the lower mantle (*1–4*). Experimental and theoretical studies of the ambient elastic moduli indicate that $MgSiO_3$ perovskite has an anomalously high shear modulus G, which requires a large temperature derivative of G to satisfy seismic velocities in the lower mantle with reasonable petrological models (*5, 6*).

In the absence of sufficiently large specimens for acoustic techniques, static compression studies have been employed to determine the isothermal bulk modulus K_T, the pressure and temperature derivatives of K_T, and thermal expansion α for silicate perovskite. Discrepancies in α and $(\partial K_T/\partial T)_P$ resulted in different lower mantle bulk compositions. The lower values of α and $|(\partial K_T/\partial T)_P|$ (*7*) favor a chemically uniform mantle with a composition similar to pyrolite (*8*) [Si/(Mg + Fe) = 0.69], whereas analyses based on the higher values of α and $|(\partial K_T/\partial T)_P|$ (*9*) favor a hotter, heterogeneous lower mantle that is enriched in silica [Si/(Mg + Fe) ~ 1]. To determine which model might be more realistic, we measured the pressure and temperature dependence of G of $MgSiO_3$ perovskite, which allows us to constrain the possible temperature and chemical composition of the lower mantle more precisely.

Polycrystalline samples of $MgSiO_3$ perovskite were synthesized in a uniaxial split-sphere apparatus at pressures above 24 GPa and at temperatures around 1700 K, for run durations between 0.5 and 3 hours. By modifying the existing 10-mm octahedral cell assembly (*10*) to maximize the sample volume and to produce minimal temperature gradients, we were able to recover cylindrical specimens that were ~1.5 mm in diameter and thickness, suitable for ultrasonic experiments with bulk densities within 2% of the single-crystal x-ray values (Table 1).

Monochromatic x-ray diffraction spectra from the polished tops and bottoms of the cylinders contained only perovskite peaks (*11*). Each sample was thoroughly examined from the ends and sides of the cylinders with microfocus Raman spectroscopy (*12*), and the best three samples of structurally pure, polycrystalline perovskites were chosen for subsequent high-pressure acoustic experiments. After polishing the cylinders under liquid nitrogen cooling, we performed acoustic tests at high pressures to confirm that the propagation of 20- to 70-MHz signals was possible through the samples.

With a recently developed technique (*13*), ultrasonic interferometric measurements of the shear elastic properties of the three samples were performed over a range of pressure and temperature (Fig. 1). The experimental paths consisted of initial compression at room temperature followed by a series of heating and cooling cycles as pressure was slowly decreased. The in situ acoustic and x-ray diffraction measurements were performed simultaneously at high pressure and at high temperature.

At each pressure and temperature for which travel times (*14*) were measured, energy-dispersive x-ray diffraction patterns from the sample and from the NaCl-confining media were col-

Table 1. Density ρ, G, and the derivatives of G from ultrasonic measurements of polycrystalline samples of $MgSiO_3$ perovskite.

Data source	ρ (10^3 kg/m^3)	G (GPa)	$(\partial G/\partial P)_T$	$-(\partial G/\partial T)_P$ (10^{-2} GPa/K)
Sample 2997	4.03(2)	175(12)	1.8(1)	3.0(1)
Sample 3020	4.06(2)	176(5)	1.9(3)	2.9(2)
Sample 3081	4.10(2)	174(7)	1.8(4)	2.8(3)
Other studies	4.107*	177(4)†	1.6–2.2‡	2.0–3.5§

*$MgSiO_3$ x-ray density from Joint Commission on Powder Diffraction Standards card 341216. †$MgSiO_3$ single-crystal Brillouin-scattering measurements (*6*). ‡Elasticity systematics of $\partial G/\partial P$ versus K_S/G for $MgSiO_3$ perovskite (*15*). §Temperature-averaged $\partial G/\partial T$ values of the lower mantle (*5*).

Y. D. Sinelnikov and R. C. Liebermann, Center for High Pressure Research and Department of Geosciences, State University of New York at Stony Brook, Stony Brook, NY 11794–2100, USA. G. Chen and M. T. Vaughan, Center for High Pressure Research and Mineral Physics Institute, State University of New York at Stony Brook, Stony Brook, NY 11794–2100, USA. D. R. Neuville, Laboratoire de Physique des Geomateriaux, Institut de Physique du Globe, 4 Place Jussieu, 75252 Paris Cedex 05, France.

*To whom correspondence should be addressed.

lected. The sample patterns provided structural information complementary to the information obtained from the microfocus Raman studies, and the NaCl patterns provided the pressure standard. The temperature was measured with two thermocouples (W/Re26%-W/Re5%) inserted opposite to each other into a salt layer adjacent to the sample.

Because the travel time measurements were made outside the thermodynamic stability field of the $MgSiO_3$ perovskite samples, the maximum temperature was limited to 800 K at the highest attained pressure to avoid retrogressive transformation. After recovery, all samples were examined with a combination of x-ray diffraction, Raman spectroscopy, density, and length measurements. In the first sample (2997) recovered from 800 K, a small amount (<10%) of orthoenstatite was detected by microfocus Raman spectroscopy. In the subsequent two experiments with samples 3020 and 3081, the maximum temperature was kept below 600 K, and no irreversible changes were detected for these samples.

Assuming hydrostatic compression, the travel times were converted to shear velocities and moduli with the equation-of-state coefficients from Wang *et al.* (*15*), who performed a static compression study of $MgSiO_3$ perovskite in the SAM-85 apparatus over a comparable pressure and temperature range (*16*). The calculated specimen lengths at high pressure and high temperature were compatible with the specimen lengths that were determined from the in situ x-ray diffraction observed in our study. The G values that we calculated (Fig. 2) as a function of pressure at temperatures from 300 to 800 K were fit as linear functions of pressure and temperature, which resulted in the values of G and the derivatives of G (Table 1). By averaging the parameters for the three experiments, we obtained the pressure and temperature derivatives of G: $(\partial G/\partial P)_T = 1.8(4)$ and $(\partial G/\partial T)_P = -0.9(3) \times 10^{-2}$ GPa/K. (Numbers in parentheses are uncertainties in measured parameters.)

The three ultrasonic experiments on $MgSiO_3$ perovskite produced results for G and the derivatives of G that were consistent with previous measurements or predictions (Table 1). The experimental G values are consistent with those obtained by averaging the single-crystal elastic moduli that were measured by Brillouin scattering. The $(\partial G/\partial P)_T$ and $(\partial G/\partial T)_P$ values agree with elasticity systematics estimates (*1*). Our $(\partial G/\partial P)_T$ value is similar to the recent measurement for $ScAlO_3$ perovskite, which is sometimes regarded as the most similar analog for $MgSiO_3$ perovskite because of the similarities in the ionic radii of the cations (*17*); however, our value of $(\partial G/\partial P)_T$ is higher than the high-temperature $(\partial G/\partial P)_T$ that is inferred for the lower mantle by Stacey (*18*).

The measured G of $MgSiO_3$ perovskite at ambient conditions is higher than the G that was modeled for a hot, adiabatically decompressed lower mantle (*4, 5*). To reconcile the high measured value of G with the value of G for a lower mantle of pyrolite (*8*) at a potential temperature of 1600 K at the foot of the mantle adiabat, Jackson (*4*) found the average $|(\partial G/\partial T)_P|$ value of 2×10^{-2} to 2.5×10^{-2} GPa/K. From the radial and lateral variations of the seismic wave velocities in the lower mantle, Wang and Weidner (*5*) deduced the temperature-averaged value of $|(\partial G/\partial T)_P|$ to be 2×10^{-2} to 3.5×10^{-2} GPa/K, which is consistent with a pyrolite compositional model; compositions that are more silicic require a larger $|(\partial G/\partial T)_P|$ value of $\sim 5.5 \times 10^{-2}$ GPa/K. In contrast, Zhao and Anderson (*19*) found that a $|(\partial G/\partial T)_P|$ value of 3.5×10^{-2} GPa/K was compatible with a wide range of perovskite-rich compositions. An indirect constraint on the value of $|(\partial G/\partial T)_P|$ comes from seismic tomography studies, which have shown a significant correlation (*20*) between heterogeneity in compressional wave (V_p) and shear wave (V_s) speeds. Karato (*21*) argued that anelastic effects are required to explain the large values of $[(\partial \ln V_s)/(\partial \ln V_p)]_P$ observed in the lower mantle. However, Wang and Weidner (*5*) showed that lateral variations in V_p and V_s can be explained as being solely due to temperature fluctuations that give the temperature-averaged $|(\partial G/\partial T)_P|$ value of about 3×10^{-2} to 4.3×10^{-2} GPa/K for a pyrolite mantle. Our measured value of $|(\partial G/\partial T)_P|$ is 2.9×10^{-2} GPa/K at high frequency (10^7 Hz) and supports the conclusion that anharmonic processes are sufficient to account for the $[(\partial \ln V_s)/(\partial \ln V_p)]_P$ value that was observed at seismic frequencies (on the order of 1 Hz), without invoking anelastic processes.

We have calculated the bulk modulus K_s and G at high temperatures and ambient pressure for a suite of compositional models and compared them with the values inferred for the hot, adiabatically decompressed lower mantle (*4, 5*) [$K_0(T) = 213(10)$ and $G_0(T) = 130(5)$ GPa] as a function of the Si/(Mg + Fe) ratio and the potential temperature. Our model lower mantle consisted of a mixture of silicate perovskite and magnesiowüstite [(Mg,Fe)O]; the total iron content was fixed at Fe/(Mg + Fe) = 0.12 (*3, 5*), and appropriate corrections were applied to the densities of perovskite and magnesiowüstite and elastic properties of magnesiowüstite (*6, 15*).

The possible mantle models demonstrate the tradeoff between the Si/(Mg + Fe) ratio and the potential temperature (Fig. 3). Higher temperatures are associated with higher Si/(Mg + Fe) ratios. For the lower values of α and $(\partial K/\partial T)_P$, which were determined in multianvil and diamond-anvil cell experiments on $MgSiO_3$ perovskite (*7*), the solutions for

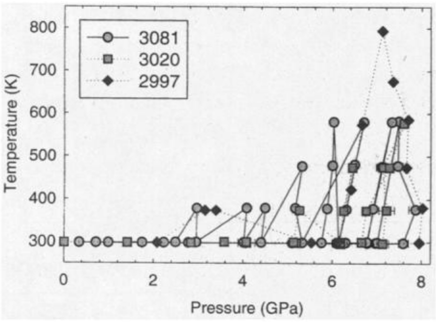

Fig. 1. The pressure-temperature experimental paths. Compression at room temperature was followed by a series of heating and cooling cycles as pressure was slowly decreased. Different symbols correspond to experiments with different samples.

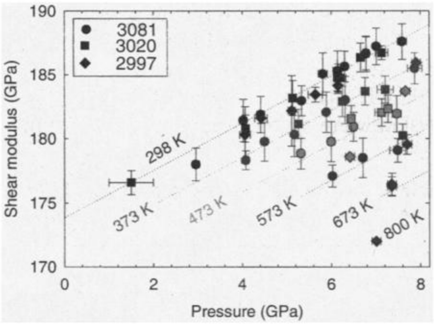

Fig. 2. Shear modulus versus pressure and temperature for three different $MgSiO_3$ perovskite polycrystalline specimens. Different symbols correspond to experiments with different samples; shading indicates different temperatures (*14*). Error bars indicate uncertainties in measured values of *G*.

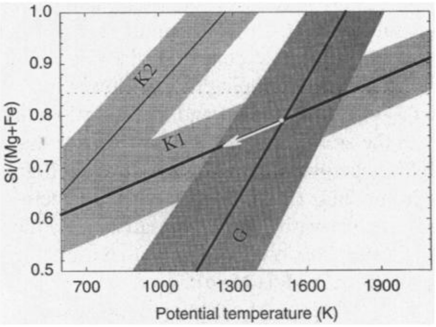

Fig. 3. Solutions for the Si/(Mg + Fe) ratio and the potential temperature at the foot of the adiabat for the lower mantle from comparison of model calculations with values inferred for the hot, adiabatically decompressed lower mantle of $K_0(T) = 213(10)$ GPa and $G_0(T) = 130(5)$ GPa (*4, 5*). Upper and lower dotted horizontal lines indicate C1 chondrite composition and pyrolite composition, respectively (*22*). Bands K_1 and K_2 represent solutions for the higher (*9*) and lower (*7*) set of experimental values of α and $(\partial K/\partial T)_P$; those for solution *G* are based on the new data reported in this study. The widths of bands K_1, K_2, and *G* reflect the uncertainties in the adiabatically decompressed mantle properties and in the experimental measurements. The arrow at the insertion of *G* and K_1 indicates the effect of adding 10 mol% Fe to the perovskite component.

the bulk and shear moduli (bands K_1 and G in Fig. 3) of the lower mantle intersect at a potential temperature $T \approx 1500$ K and Si/(Mg + Fe) ≈ 0.78, a value between the values for pyrolite (*8*) and Cl carbonaceous chondritic meteorites (*22*). Within the model uncertainties, pyrolitic and chondritic models are permissible, but pure enstatite (perovskite with no magnesiowüstite) models are not. For the higher values of α and $(\partial K/\partial T)_P$ that were determined in diamond-anvil experiments on $(\mathrm{Mg,Fe})\mathrm{SiO}_3$ perovskite (*9*), there were no allowable (no intersection of the K_2 and G bands) solutions in the compositional range between pure olivine and pure enstatite models and the potential temperature range between 600 and 2100 K. The uncertainty of 10% in the measured value of $(\partial G/\partial T)_P$ results in variations of ±0.02 in the Si/(Mg + Fe) ratio and variations of ±100 K in temperature. Adding Fe of 10 mole percent (mol%) to the perovskite phase in the model calculations (*23*) decreases G (by 8%), thus leading to lower potential temperatures and to compositions that are more olivine-rich.

References and Notes

1. T. S. Duffy and D. L. Anderson, *J. Geophys. Res.* **94**, 1895 (1989).
2. R. Jeanloz and E. Knittle, *Philos. Trans. R. Soc. London Ser. A* **328**, 377 (1989).
3. R. J. Hemley *et al.*, in *High-Pressure Research: Application to Earth and Planetary Sciences*, Y. Syono and M. H. Manghnani, Eds. (American Geophysical Union, Washington, DC, 1992), pp. 183–189.
4. I. Jackson, *Geophys. J. Int.* **134**, 291 (1998).
5. Y. Wang and D. J. Weidner, *Pure Appl. Geophys.* **146**, 533 (1996).
6. A. Yeganeh-Haeri, *Phys. Earth Planet. Inter.* **87**, 111 (1994); A. Yeganeh-Haeri, D. J. Weidner, E. Ito, *Science* **243**, 787 (1989).
7. The values are $\alpha \approx 2 \times 10^{-5}$/K and $|(\partial K_T/\partial T)_P| \approx 2 \times 10^{-2}$ GPa/K [for example, (*15*); W. Utsumi *et al.*, *Geophys. Res. Lett.* **22**, 1005 (1995); N. Funamori *et al.*, *J. Geophys. Res.* **101**, 8257 (1996); G. Fiquet *et al.*, *Phys. Earth Planet. Inter.* **105**, 21 (1998)].
8. The primitive mantle material called pyrolite was proposed by A. E. Ringwood [*Composition of the Earth's Mantle* (McGraw-Hill, New York, 1975), p. 295] to produce a typical basaltic magma on fractional melting. The initially proposed composition was one part of basalt and four parts of dunite.
9. The values are $\alpha \approx 4 \times 10^{-5}$/K and $|(\partial K/\partial T)_P| \approx 5 \times 10^{-2}$ GPa/K [for example, (*2*); E. Knittle *et al.*, *Nature* **319**, 214 (1986); H. K. Mao *et al.*, *J. Geophys. Res.* **96**, 8069 (1991); L. Stixrude, R. J. Hemley, Y. Fei, H. K. Mao, *Science* **257**, 1099 (1992)].
10. T. Gasparik, *J. Geophys. Res.* **95**, 15751 (1990).
11. From visual examination, perovskite specimens consisted of relatively large (up to 30 μm), transparent, colorless grains; finely polished surfaces revealed grain boundaries in equilibrium and an absence of twinning.
12. P. F. McMillan *et al.*, in *Mineral Spectroscopy: A Tribute to Roger G. Burns*, M. D. Dyar, C. McCammon, M. W. Schaefer, Eds. (Geochemical Society, Washington, DC, 1996), pp. 175–190.
13. Recently, we have adapted ultrasonic interferometry techniques to a DIA-type, cubic anvil, high-pressure apparatus (SAM-85) installed on the superconducting wiggler beamline (X17B1) at the National Synchrotron Light Source of the Brookhaven National Laboratory [G. Chen, R. C. Liebermann, D. J. Weidner, *Science* **280**, 1913 (1998)].
14. In ultrasonic interferometry, a burst of high-frequency signal is applied to the piezoelectric transducer. The resultant elastic wave, propagating inside the sample, produces a series of echoes. The travel time of an elastic wave through the sample is measured by observing constructive and destructive interferences among overlapped echoes as a function of carrier frequency.
15. Y. Wang *et al.*, *Phys. Earth Planet. Inter.* **83**, 13 (1994).
16. The largest uncertainties in travel times (±1%) originated from the anomalous travel-time dispersion. To minimize this dispersion, we chose a sufficiently large frequency window in our interference data, over which all collected travel times had a comparable dispersion shape. The travel times were averaged over a chosen frequency window to obtain G as a function of pressure and temperature. Discrepancies occurred for the data collected under initial compression at room temperature because of nonhydrostatic stresses. The deviation from hydrostatic conditions was accounted for by estimating pressures from subsets {200, 420} and {222, 220} of salt diffraction lines and by assigning the corresponding difference to a pressure uncertainty of the measurements.
17. J. Kung, thesis, Australian National University, Canberra (1997); J. Kung and S. M. Rigden, *Eos Trans. Am. Geophys. Union, Fall Meet. Suppl.* **78**, F803 (1997).
18. F. D. Stacey, *Phys. Earth Planet. Inter.* **89**, 219 (1995).
19. Y. Zhao and D. L. Anderson, *ibid.* **85**, 273 (1994).
20. Seismic tomography studies have shown that $[(\partial \ln V_s)/(\partial \ln V_p)]_P \approx 2$ throughout the lower mantle [for example, A. Hales and H. Doyle, *Geophys. J. R. Astron. Soc.* **13**, 403 (1967); J. Woodhouse and A. Dziewonski, *Philos. Trans. R. Soc. London Ser. A* **328**, 291 (1989); X. Li *et al.*, *Geophys. J. Int.* **105**, 649 (1991); G. Robertson and J. Woodhouse, *ibid.* **123**, 85 (1995)].
21. S. Karato, *Geophys. Res. Lett.* **20**, 1623 (1993).
22. W. F. McDonough and S.-s. Sun, *Chem. Geol.* **120**, 223 (1995).
23. The inclusion of Fe was assumed to reduce perovskite's G in a manner similar to the reduction of G in magnesiowüstite (*5*, *6*).
24. We thank the personnel who contributed to the execution of these ultrasonic experiments in SAM-85 at the National Synchroton Light Source (NSLS) of the Brookhaven National Laboratory: H. Kagi, J. Liu, H. Schay, K. Baldwin, P. Hoversen, B. Vitale, C. Koleda, and B. Huebsch. We especially thank Y. Fei and B. Mysen at the Geophysical Laboratory for helping with the Raman spectroscopy measurements; J. Hastings and D. Siddons at the NSLS for their technical support at the beamline X17B1, where this work was performed; J. Chen and D. Weidner for their support and encouragement in this new project; and Y. Wang for providing the pressure-volume-temperature data. These high-pressure experiments were conducted with the joint support of the State University of New York at Stony Brook and the NSF Science and Technology Center for High Pressure Research under Earth Sciences Division grant EAR 89-20239. This research was also supported by NSF grants to R.C.L. (EAR 93-04502 and 96-14612). This is Mineral Physics Institute contribution 226.

30 March 1998; accepted 16 June 1998

Multi-Atom Resonant Photoemission: A Method for Determining Near-Neighbor Atomic Identities and Bonding

A. Kay, E. Arenholz, S. Mun, F. J. García de Abajo,* C. S. Fadley,†
R. Denecke,‡ Z. Hussain, M. A. Van Hove

Measurements and theoretical calculations are reported for an interatomic multi-atom resonant photoemission (MARPE) effect that permits direct determination of near-neighbor atomic identities (atomic numbers). MARPE occurs when the photon energy is tuned to a core-level absorption edge of an atom neighboring the emitting atom, with the emitting level having a lower binding energy than the resonant level. Large peak-intensity enhancements of 33 to 105 percent and energy-integrated effects of 11 to 29 percent were seen in three metal oxides. MARPE should also be sensitive to bond distance, bonding type, and magnetic order, and be observable via the secondary processes of x-ray fluorescence and Auger decay.

Several experimental techniques presently permit determining the bulk atomic structures of solids, including x-ray diffraction and extended x-ray absorption fine structure (EXAFS) (*1*). EXAFS is also element-specific via core-level electronic excitations and allows the local structure around each atomic type to be determined, specifically the radial positions of shells of neighboring atoms. If the atomic structure near solid surfaces is to be probed, then low energy electron diffraction (LEED) (*2*) and photoelectron diffraction (PD) (*3*) can be added to this list, with the latter also being element-specific via core excitation. However, as powerful and widely used as the aforementioned methods are, none of them permits directly determining the type of atom that neighbors a given atom. That is, some of these techniques (such as EXAFS and PD) may be element-specific for the central atom in the structure, but there is no simple way to determine the near-neighbor atomic identities (atomic numbers) from them. Use can be made of the differences in electron–atom scattering strengths between different atoms in these last two methods, together with comparison of experiment with model calculations, but this is only unambiguous when